

Suitability of using far-infrared imaging system for noncontact evaluation on working state of implantable medical devices

Yang Yang,¹ Xiao-Juan Wei,¹ and Jing Liu^{1,2,a)}

¹Key Laboratory of Cryogenics, Technical Institute of Physics and Chemistry, Chinese Academy of Sciences, Beijing 100190, People's Republic of China

²Department of Biomedical Engineering, School of Medicine, Tsinghua University, Beijing 100084, People's Republic of China

(Received 17 June 2008; accepted 2 February 2009; published online 25 March 2009)

The far-infrared thermal imaging is a promising noncontact way to assess the working state of an implantable medical device (IMD). The unique merit of this method lies in its direct detection of the unusual skin surface temperature distribution caused by the implanted IMD. This paper is dedicated to present a comprehensive investigation on the suitability of using far-infrared system to evaluate the thermal state at the skin surface above the implantation location of the IMD under various working, physiological, or environmental thermal conditions. It was found that an evident variation in temperature as disclosed on the skin surface is beneficial for the far-infrared thermal imaging detection. In addition, numerical simulations were also performed on three dimensional bioheat transfer problems in human bodies embedded with IMD by different implantation depth and physical characteristics. Both theoretical analysis and numerical simulation indicated that for a specific image system with fixed temperature resolution, when the IMD is embedded as close as possible to the superficial skin, the abnormal region of temperature on skin surface can be much more visible. Conceptual experiments either *in vitro* or *in vivo* are implemented to preliminarily demonstrate the theoretical predictions. To further improve the detection of an implanted IMD, intentional cooling by the alcohol was proposed and evaluated. Given the fact that several information of an implanted IMD can be revealed through the infrared thermograph, such noncontact imaging method could serve well as an assessment approach without causing any wound and radiation to human body. © 2009 American Institute of Physics. [DOI: 10.1063/1.3093868]

I. INTRODUCTION

Implantable medical devices (IMDs) are the instruments which can be fully or partially inserted into a human body or body cavity for permanent use by a medical intervention.¹ Some of the IMDs have already been very familiar to us, such as cardiac pacemaker; cardiac defibrillator; cochlear implant; pain, muscle, bladder, sphincter, or respiration stimulators; insulin or drug pumps; and electrocardiogram, pressure, and other implantable monitors.¹⁻⁶ Their distinct clinical role is not only to enhance or replace certain function of a specific tissue or organ in human body but also to monitor special physiological parameters of human body. In fact, such devices have already been beneficial for both the patient and the healthy people who wish to adopt them to expand his physiological limit in the near future.⁷ Therefore, the IMDs have been very common and extremely important today as a part of modern advanced medical technologies and have increasingly prevailed throughout the world.⁸

It is obvious that the IMDs link much closer with the human life and health as each day passes by, so the security, stability, reliability, and running state assessments of the IMDs are of great importance. After implantation, the assessment of an IMD should be concentrated on the following aspects: implantation location, shell soundness, compatibility

with the surrounding tissue, the running state, the battery power loss, and so on.⁹⁻¹⁶ Up to now, the most commonly used diagnostic method is to observe clinical symptoms of the person who has been implanted with IMD.^{3,13-16} At the same time, employing the monitoring instruments of human physiological parameters can also help administer the assessments.^{17,18} With the aid of observation and signal outputs, the doctor can directly conclude whether the IMD is under normal running state and producing a desired effect. Otherwise, medical imaging can also achieve some assessments of the IMD. Implantation location, shell soundness, and the compatibility with the surrounding tissue of the IMD can be directly indicated on the image.^{9,10,19-21} For those IMDs who possess electrical energy, sufficient electrical capacity is the guarantee of normal running state of the IMDs.^{3,6} Two major methods for battery capacity checking are, respectively, the direct check of the battery relying on the surgical and the battery management system (BMS) integrated with the IMD which can monitor the status of the battery and send out the alert signals before battery runs out.^{3,22}

However, all of these assessment methods owe their own insurmountable limitations and shortcomings. For example, the appearance of abnormal clinical symptoms or monitoring signals means grave danger while the IMD is implanted to maintain the patient's life. If the doctor offered inaccurate judgment or treatment at the moment, it will lead to serious consequence. Many commonly adopted advanced imaging

^{a)}Author to whom correspondence should be addressed. Electronic mail: jliu@mail.ipc.ac.cn. Tel. 8610-82543765.

systems in clinics such as x-ray computer tomography (X-CT), ultrasound, or magnetic resonance imaging (MRI) may cause potential danger to the patient due to their interaction with the body inside IMD. Besides, they are mainly structure sensitive and generally incapable of determining the running state of the IMD, let along the operating cost of the imaging equipment be extremely high. Further, when checking on the battery capacity, surgical operation will cause people great suffering and BMS will consume battery power which further shortens the service life of IMD.

Aiming to partially address the above difficulties, this paper is dedicated to propose an alternative strategy for IMD assessment which employs the conventional instrument for surface temperature detection, namely, the far-infrared thermal imaging system. Based on this strategy, the far-infrared thermal imaging system is employed to detect the unique temperature distribution on the skin surface caused by the implanted IMD. The main assessment aspects of the implanted IMD can be deduced from the infrared thermographs, such as the implantation location and depth, the outline of the shell, the compatibility with surrounding tissue, and so on. Once there is something abnormal occurs, it will be directly displayed on the infrared thermographs which will lead us to find out the correlation information. This strategy allows a completely safe and effective noncontact evaluation on working state of the IMD. The theoretical analysis and numerical simulation proposed in this paper have revealed that, because of the heat generation of the IMD during working and the undeniable differences in thermal parameter between IMD and human body, the temperature of skin surface at the implantation location appears distinct from surrounding tissue. Further parametric evaluation demonstrates that much information about the implanted IMD can be disclosed and concluded by the skin surface temperature distribution, which means that the assessment of the IMD can be achieved by the far-infrared thermal imaging system. A series of experiments was also performed to verify such far-infrared thermal imaging method. Such efforts have not been carried out before.

II. THEORETICAL ANALYSIS

A. Biological heat transfer model for living tissue implanted with IMD

In order to find out the temperature difference on skin surface between the implantation location and surrounding tissue, a generalized biological heat transfer model for living tissue implanted with IMD is established. To characterize the heat transfer in the living tissues, we adopted the well-known Pennes bioheat equation²³ which describes the influence of blood flow on the temperature distribution in the tissue in terms of volumetrically distributed heat sinks or sources. For the IMD, because of its heat generation during the working process and the typical implanting pattern, it can be simplified as a point-heating source due to its much smaller volume compared with human body. At the same time, its thermal impact on the whole human body is limited. Therefore, for the sake of simplification, we have chosen a local three dimensional (3D) cube in human body as the analyzed spatial

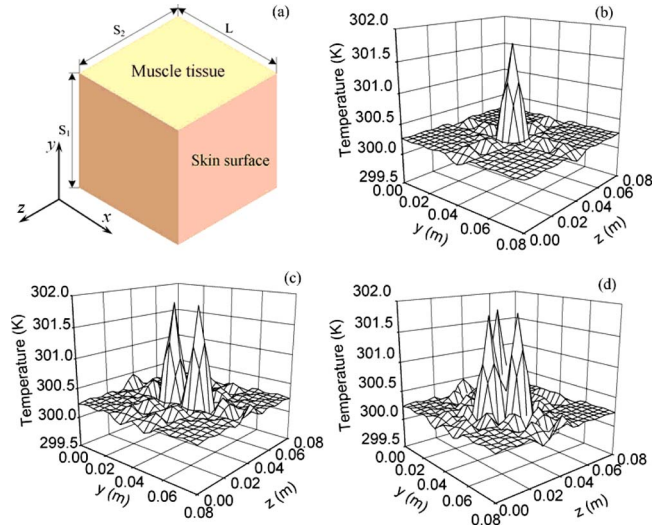


FIG. 1. (Color online) (a) Sketch about the 3D cubic calculation domain with a size of $S_1 \times S_2 \times L$, (b) steady-state temperature distribution at the skin surface embedded with single IMD, (c) steady-state temperature distribution at the skin surface embedded with two IMDs, and (d) steady-state temperature distribution at the skin surface embedded with three IMDs.

domain and defined the IMD as a point-heating source. And 3D biological heat transfer model for living tissue implanted with the IMD can be established as

$$\rho c \frac{\partial T(X,t)}{\partial t} = k \nabla^2 [T(X,t)] + \omega_b \rho_b c_b [T_a - T(X,t)] + Q(X,t), \quad X \in \Omega, \quad (1)$$

where $Q(X,t) = Q_m(X,t) + Q_r \delta(X_1 - X)$; $T(X,t)$ is the tissue temperature and Q_m is the metabolic heat generation rate; ρ and c are, respectively, the density and specific heat of living tissue; ρ_b , c_b , and ω_b denote density, specific heat, and perfusion rate of blood; k is the thermal conductivity of tissue; T_a is the arterial temperature which is often treated as a constant; Ω signifies the analyzed spatial domain which is a 3D cube with widths S_1 and S_2 and height L ; X contains the Cartesian coordinates x , y , and z , where x denotes the tissue depth from the body core while y and z are coordinates along the surface [Fig. 1(a)]; Q_r and X_1 are, respectively, the point-heating source intensity and the implanted location of the IMD; and $\delta(X)$ is the delta function.

The boundary conditions for the point-IMD implantation pattern as shown in Fig. 1(a) are prescribed as follows:

$$\begin{aligned} -k \frac{\partial T(x,y,z,t)}{\partial y} &= 0 \quad \text{at } y=0, \\ -k \frac{\partial T(x,y,z,t)}{\partial y} &= 0 \quad \text{at } y=S_1, \end{aligned} \quad (2)$$

$$\begin{aligned} -k \frac{\partial T(x,y,z,t)}{\partial z} &= 0 \quad \text{at } z=0, \\ -k \frac{\partial T(x,y,z,t)}{\partial z} &= 0 \quad \text{at } z=S_2, \end{aligned} \quad (3)$$

$$T(x, y, z, t) = T_c \quad \text{at } x = 0,$$

$$-k \frac{\partial T(x, y, z, t)}{\partial x} = h_f(T_f - T) \quad \text{at } x = L, \quad (4)$$

where the skin surface is defined at $x=L$ while the body core at $x=0$, h_f is the apparent heat convection coefficient between the skin surface and the surrounding air under physiologically basal state and is an overall contribution from natural convection and radiation, and T_f is the surrounding air temperature. The reason for adopting the adiabatic conditions on the boundaries along the y and z directions is based on the consideration that at the positions far from the center

of the domain, the temperature field is almost not affected by the central domain or external heating/cooling.

The initial condition is defined as²⁴

$$T(x, y, z, 0) = T_0(x, y, z). \quad (5)$$

Associate with boundary conditions [Eqs. (2)–(4)] and initial conditions, the solution to Eq. (1) can be obtained as^{25,26}

$$T(x, y, z, t) = T_0(x, y, z) + W(x, y, z, t) \exp\left(-\frac{\omega_b \rho_b c_b}{\rho c} t\right), \quad (6)$$

where

$$T_0(x, y, z) = T_a + \frac{Q_m}{\omega_b \rho_b c_b} + \frac{\left(T_c - T_a - \frac{Q_m}{\omega_b \rho_b c_b}\right) \left\{ \sqrt{A} ch[\sqrt{A}(L-x)] + \frac{h_f}{k} sh[\sqrt{A}(L-x)] \right\}}{\sqrt{A} ch(\sqrt{A}L) + \frac{h_f}{k} sh(\sqrt{A}L)} + \frac{\frac{h_f}{k} \left(T_f - T_a - \frac{Q_m}{\omega_b \rho_b c_b}\right) sh(\sqrt{A}x)}{\sqrt{A} ch(\sqrt{A}L) + \frac{h_f}{k} sh(\sqrt{A}L)}, \quad (7)$$

$$W(x, y, z, t) = \frac{\alpha}{k} \int_{\tau=0}^t d\tau \int_{x'=0}^L \int_{y'=0}^{S_1} \int_{z'=0}^{S_2} G(x, y, z, t; x', y', z', \tau) Q_i \delta(X'_1 - X') \exp\left(\frac{\omega_b \rho_b c_b}{\rho c} \tau\right) dx' dy' dz'$$

$$+ \alpha \int_{\tau=0}^t d\tau \int_{y'=0}^{S_1} \int_{z'=0}^{S_2} G(x, y, z, t; x', y', z', \tau) \Big|_{x'=L} \frac{h_f}{k} g(\tau) dy' dz', \quad (8)$$

$$G(x, y, z, t; x', y', z', \tau) = \sum_{m=1}^{\infty} \sum_{n=0}^{\infty} \sum_{p=0}^{\infty} c_{mnp} e^{-\alpha(\beta_m^2 + \gamma_n^2 + \eta_p^2)(t-\tau)} \sin \beta_m x \cos \gamma_n y \cos \eta_p z \sin \beta_m x' \cos \gamma_n y' \cos \eta_p z', \quad (9)$$

$$g(t) = \left[\frac{k}{h_f} \frac{\partial T_0(x, y, z)}{\partial x} \Big|_{x=L} - T_0(x, y, z) \Big|_{x=L} + T_f \right] \exp\left(\frac{\omega_b \rho_b c_b}{\rho c} t\right) H(t), \quad (10)$$

$$c_{mnp} = \frac{2[\beta_m^2 + (h_f/k)^2] R_1 R_2}{\{L[\beta_m^2 + (h_f/k)^2] + h_f/k\} S_1 S_2}, \quad (11)$$

and $A = \omega_b \rho_b c_b / k$; $\alpha = k / \rho c$;

$$H(t) = \begin{cases} 0, & t < 0 \\ 1, & t > 0 \end{cases}$$

is the Heaviside function; $\gamma_{n-1} = n\pi/S_1$, $n=0, 1, 2, 3, \dots$; $\eta_{p-1} = p\pi/S_2$, $p=0, 1, 2, 3, \dots$;

$$R_1 = \begin{cases} 1 & n = 0 \\ 2 & n = 1, 2, 3, \dots \end{cases}$$

$$R_2 = \begin{cases} 1 & p = 0 \\ 2 & p = 1, 2, 3, \dots \end{cases}$$

and β_m are positive roots of the following equation:

$$\beta_m \cot \beta_m L = -h_f/k. \quad (12)$$

Here, only the final solution form was given for brief. For a specific procedure to derive the above solutions, readers are referred to Refs. 25 and 26 for more details.

When several IMDs are embedded in different locations of the human body, the expression $Q_i \delta(X_i - X)$ in Eq. (8) can be substituted by $\sum_i Q_i \delta(X_i - X)$, where i , X_i , and Q_i , respectively, imply the sequence number, implantation location, and point-heating source intensity of the IMDs.

TABLE I. Temperature difference on the skin surface between the central location of IMD and surrounding tissue with different implantation depths in the theoretical analysis.

Position of IMD (m)	0.02	0.04	0.05	0.06	0.075
Temperature difference (K)	4×10^{-3}	-0.11	0.246	0.042	1.514

For single IMD implantation, when $t \rightarrow \infty$, the steady-state solution to Eq. (1) can be expressed as

$$T(x,y,z) = T_0(x,y,z) + \frac{\alpha Q_r}{k} \sum_{m=1}^{\infty} \sum_{n=0}^{\infty} \sum_{p=0}^{\infty} \frac{c_{mnp} \sin \beta_m x \cos \gamma_n y \cos \eta_p z \sin \beta_m x'_1 \cos \gamma_n y'_1 \cos \eta_p z'_1}{\alpha(\beta_m^2 + \gamma_n^2 + \eta_p^2) + \frac{\omega_b \rho_b c_b}{\rho c}} + \frac{B h_f}{\rho c} \sum_{m=1}^{\infty} \frac{c_{mnp} S_1 S_2 \sin \beta_m x \sin \beta_m L}{\alpha \beta_m^2}, \quad (13)$$

where

$$B = \frac{-2\sqrt{A} \left(T_c - T_a - \frac{Q_m}{\omega_b \rho_b c_b} \right) + \left(T_f - T_a - \frac{Q_m}{\omega_b \rho_b c_b} \right) \left(\sqrt{A} ch(\sqrt{AL}) - \frac{h_0}{k} sh(\sqrt{AL}) \right)}{\sqrt{A} ch(\sqrt{AL}) + \frac{h_0}{k} sh(\sqrt{AL})} + T_f - T_a - \frac{Q_m}{\omega_b \rho_b c_b}. \quad (14)$$

B. Temperature distribution on the skin surface

Based on the above theoretical solution, the steady-state temperature distribution along the skin surface can be further calculated as

$$T(L,y,z) = T_0(L,y,z) + B h_f \sum_{m=1}^{\infty} \frac{c_{mnp} S_1 S_2 \sin \beta_m L \sin \beta_m L}{k \beta_m^2} + Q_r \sum_{m=1}^{\infty} \sum_{n=0}^{\infty} \sum_{p=0}^{\infty} \frac{c_{mnp} \sin \beta_m L \cos \gamma_n y \cos \eta_p z \sin \beta_m x'_1 \cos \gamma_n y'_1 \cos \eta_p z'_1}{k(\beta_m^2 + \gamma_n^2 + \eta_p^2) + \omega_b \rho_b c_b}. \quad (15)$$

Let the dimension of the calculation domain be $S_1=S_2=L=0.08$ m. Assuming the running voltage and impedance of the IMD to be 1.5 V and 10 k Ω ,⁷ the heat generation for each IMD is calculated as $Q=2.25 \times 10^{-4}$ W. Without losing generality, for the present qualitative assessment, the point-heating source intensity is estimated as $Q_r=0.225$ W/m³. The temperature of surrounding air at the skin surface is $T_f=303$ K, while the heat convection coefficient is $h_f=20$ W/m² K. And other thermal parameters of living tissue are defined as²⁶ $Q_m=4200$ W/m³, $k=0.5$ W/m K, $c_b=c=4200$ J/kg K, $T_a=T_c=310$ K, $\omega_b=0.05$ ml/s ml, and $\rho_b=\rho=1000$ kg/m³.

The results are given in Figs. 1(b)–1(d) which, respectively, represent the temperature distribution on the skin surface embedded with one, two, and three IMDs at the same implantation depth but different positions. It makes clear that the maximum steady-state temperatures on the skin surface occur at the positions of IMD [in Fig. 1(b), the single IMD is embedded at 0.075, 0.04, and 0.04 m; in Fig. 1(c), the two IMDs are at 0.075, 0.032, and 0.04 m and 0.075, 0.048, and 0.04 m, respectively; in Fig. 1(d), the three IMDs are at 0.075, 0.032, and 0.04 m, 0.075, 0.048, and 0.04 m, and 0.075, 0.04, and 0.028 m, respectively]. One can still observe that the temperature for the skin surface surrounding the IMDs can fairly be kept at a lower temperature on the whole. This is very beneficial for the far-infrared thermal imaging detection.

Further, the IMDs will be implanted into different locations in human body due to their distinctive function. There-

fore, the temperature distribution on the skin surface may be affected owing to the different implantation depths. Therefore, different implantation depths of one IMD have also been tested. The distances between the IMD and body core along dimension x are, respectively, prescribed as 0.02, 0.04, 0.05, 0.06, and 0.075 m. The results in Table I indicate that no matter where the implanted IMD is located, there always exists a temperature difference on the skin surface between the location of IMD and surrounding tissue. Coincidentally, the largest temperature difference is 1.514 K and occurs at the point farthest from the body core.

Based on the above theoretical result, a brief conclusion can be drawn as follows. For an implanted IMD, different locations and implanted depths can be revealed on the skin surface temperature distribution which is quite suitable for the far-infrared thermal imaging detection. Moreover, the best situation for detection should be that the IMD is embedded as close as possible to the superficial skin, where a maximum temperature difference between the position of IMD and surrounding tissue could be established. This would guarantee a good detection of IMD by the far-infrared thermal imaging system. However, for the sake of simplification, human body and IMD have been, respectively, defined as one piece of uniform medium and a point-heating source, while the complex heat transfer mode in human body and other physical characters of IMD have been ignored. Therefore, in the results, although the temperature distribution on the skin surface fits well for the far-infrared thermal imaging detection, the influence of the physical characters of the IMD

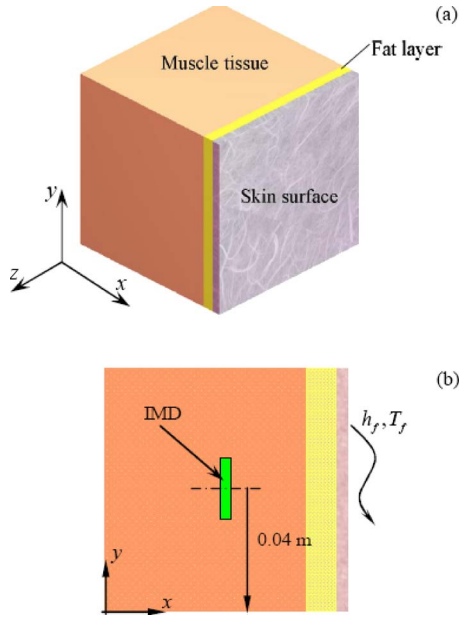


FIG. 2. (Color online) (a) Sketch of three-layer human body tissues with a size of $0.08 \times 0.08 \times 0.08 \text{ m}^3$ and (b) sketch about calculation domain embedded with IMD.

on the temperature distribution is still unknown. And then we have to establish another model which has more adaptation to many actual situations and rely on the numerical simulation for further analysis.

III. NUMERICAL SIMULATION

A. Heat transfer model and calculation domain

Although a brief evaluation on the heat transfer in human body embedded with a point IMD has already been given as above, it overall represents only a highly simplified case. A better understanding on the actual conditions requires 3D numerical simulation on the heat transfer problems of human body embedded with a 3D IMD. It would take both the geometric and the thermal physical properties of the implanted IMD into account.

For this purpose, as shown in Fig. 2(a), the human body is prescribed as a three-layer model consisting of muscle, fat, and skin, respectively. And a rectangular geometry with a dimension of $0.08 \times 0.08 \times 0.08 \text{ m}^3$ is selected for the analysis where x denotes the tissue depth from the body core while y and z are coordinates along the surface. In Fig. 2(b), the green block structure embedded in the muscle tissue denotes the IMD which was set as a $32 \times 32 \times 4 \text{ mm}^3$ thin cube.

The heat transfer in an IMD with heat generation can be described by a thermal diffusion equation

$$\rho_i c_i \frac{\partial T_i(X,t)}{\partial t} = \nabla \cdot [k_i \nabla T_i(X,t)] + Q_r, \quad (16)$$

where $T_i(X,t)$ is the device temperature; ρ_i , c_i , and k_i are, respectively, the density, specific heat, and thermal conductivity of the material of IMD; X contains the Cartesian coordinates x , y , and z ; and Q_r denotes the heat generation rate of the IMD.

The 3D Pennes equation for characterizing bioheat transfer of the surrounding tissues reads as

$$\rho c \frac{\partial T(X,t)}{\partial t} = \nabla \cdot [k(X) \nabla T(X,t)] + Q_b + Q_m, \quad (17)$$

where $T(X,t)$ is the tissue temperature distribution and $k(X)$ is the space-dependent thermal conductivity of the tissue. $Q_b = \rho_b c_b \omega_b(X) [T_a - T(X,t)]$ and $\omega_b(X)$ is the space-dependent blood perfusion. In the present model, blood perfusion and metabolic heat generation only exist in the muscle tissue.

The boundary conditions for a practical IMD implantation pattern are identical to that set up in Sec. II A. At the six interfaces between biological tissues and rectangular IMD, a continuum equation for both temperature and heat flux is adopted, i.e.,

$$T = T_i, \quad k \frac{\partial T}{\partial n} = k_i \frac{\partial T_i}{\partial n}, \quad (18)$$

where T_i and k_i are, respectively, the temperature and thermal conductivity of IMD, T and k are, respectively, the temperature and thermal conductivity of body tissue, and n is the normal direction of the tissue-TEG interface.

In the numerical calculations, the typical parameters for the tissue are set as follows:²⁶ $\rho = \rho_b = 1000 \text{ kg/m}^3$ and $c = c_b = 4200 \text{ J/kg K}$; the muscle tissue is regarded to have a thickness of 74 mm with thermal parameters as $k = 0.5 \text{ W/m K}$, $Q_m = 4200 \text{ W/m}^3$, and $\omega_b = 0.005 \text{ ml/s ml}$; the thickness of the skin is generally within the range of 0.5–4 mm and treated here as 2 mm, and its thermal conductivity is 0.3 W/m K ; the thickness of the fat layer is taken as 4 mm, and its thermal conductivity is 0.2 W/m K ; and both Q_m and ω_b in these two layers are zero. The body core temperature is equal to the arterial temperature $T_a = T_c = 310 \text{ K}$. The temperature of the surrounding air at the skin surface is $T_f = 303 \text{ K}$, while the heat convection coefficient is $h_f = 20 \text{ W/m K}$.

For the IMD part, the titanium has been selected as the material whose typical parameters are set as $\rho_i = 4850 \text{ kg/m}^3$, $c_i = 544.25 \text{ J/kg K}$, and $k_i = 7.44 \text{ W/m K}$, respectively.^{27,28} According to Sec. II B, while the running voltage and impedance of the IMD are 1.5 V and 10 k Ω , the strength of heat generation for IMD is about $Q_r = 50 \text{ W/m}^3$. Although various materials can be tested using the present method, only the above material will be analyzed for brevity.

According to Ref. 7, 3D numerical simulations coupled with the heat transfer equations in tissue and IMD were developed from the commercially available software FLUENT in the $0.08 \times 0.08 \times 0.08 \text{ m}^3$ cube with the parameters and boundary conditions given above. The temperature distribution in the whole calculation domain, especially on the skin surface, can thus be obtained. Since the method for IMD assessment presented in this paper is to detect the skin surface temperature distribution by the infrared imaging system, various simulations will be made by setting different parameters according to actual conditions to reveal the correlation between the characteristics of the skin surface temperature distribution and each property of the implanted IMD.

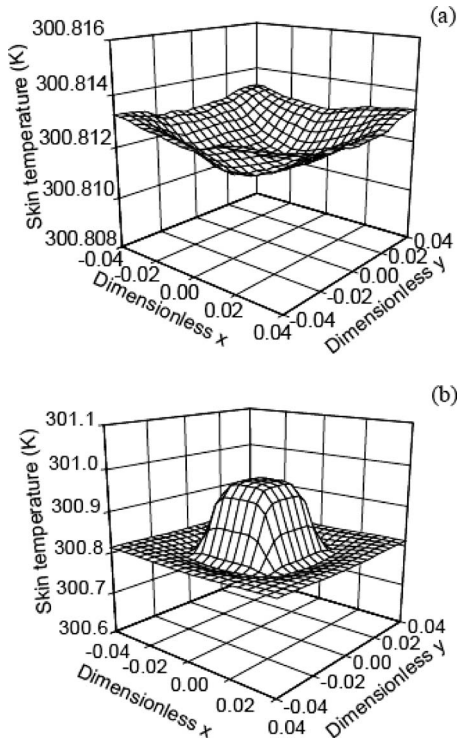


FIG. 3. Temperature distribution on the skin surface: (a) implantation depth of 0.02 m and (b) implantation depth of 0.07 m.

B. Effect of IMD characters on skin surface temperature distribution

1. Different implantation depth

Consistent with the theoretical analysis, the effect of different implantation depths on the skin surface temperature distribution has also been tested and the distances between the left side of IMD and body core along dimension *x* are, respectively, prescribed as 0.02, 0.04, 0.05, 0.06, and 0.07 m. Other parameters keep identical to each other.

The steady-state temperature distributions on the skin surface are depicted in Figs. 3(a) and 3(b), while the implantation depths are, respectively, 0.02 and 0.07 m. It is obvious that such two temperature distributions are different from each other where Fig. 3(a) is concave and Fig. 3(b) appears convex. The results in Table II indicate that the largest temperature difference occurs at the point farthest from the body core, which accords well with the theoretical result. It can be easily found that when the IMD is implanted near the body core, a low-temperature region will be present at the skin surface; when the IMD is implanted far away from the body core, a high-temperature region would emerge on the skin surface; and the further from the body core, the larger temperature difference. On the other hand, in this case, one can deduce the implantation depth of the IMD according to the distinct temperature region emerged on the skin surface: if it

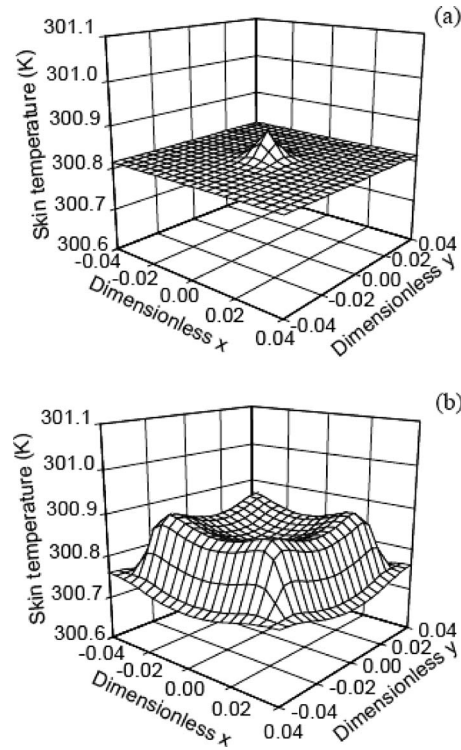


FIG. 4. Temperature distribution on the skin surface: (a) width of IMD 4 mm and (b) width of IMD 64 mm.

is a high-temperature region on the skin surface, the IMD is implanted far away from the body core; if there is a low-temperature region on the skin surface, the IMD is embedded near the body core.

Overall, in consideration of various physical properties of IMD, the maximum temperature difference between the central location of IMD and surrounding tissue has been found as 0.154 K whose value is strong enough to guarantee the detection by a far-infrared thermal imaging system. Therefore, the following calculation will be performed with the same implantation depth of 0.07 m.

2. Different IMD volume

An IMD may take on different volumes according to its specific function and design. Therefore, the skin surface temperature distribution influenced by the IMD will present different areas. In the calculation, assuming that the running voltage and impedance of the IMD are still 1.5 V and 10 kΩ, the heat generation for each IMD is 2.25×10^{-4} W. Keeping the thickness of the IMD constant as 4 mm and both widths are, respectively, set as 4, 8, 16, 32, and 64 mm, the heat generation rates for each IMD are, respectively, 3516, 879, 220, 54, and 17 W/m³. Other parameters keep identical to each other.

The results displayed in Figs. 4(a) and 4(b) are, respec-

TABLE II. Temperature difference on the skin surface between the central position of IMD and surrounding tissue with different implantation depths in the numerical simulation.

Position of IMD (m)	0.02	0.04	0.05	0.06	0.07
Temperature difference (K)	-0.0021	-5.2×10^{-4}	-6.7×10^{-4}	0.002 07	0.154 75

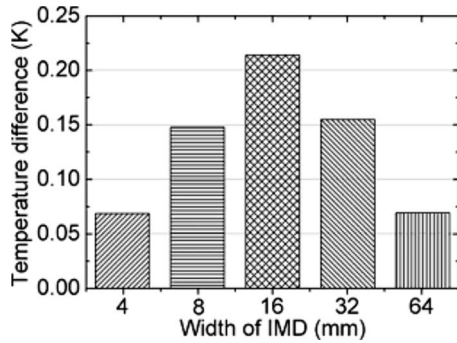


FIG. 5. Temperature difference on the skin surface between the central position of IMD and surrounding tissue with different implantation depths.

tively, the steady-state temperature distribution on the skin surface with the widths of IMD, respectively, as 4 and 64 mm. Figure 5 denotes the temperature difference on the skin surface between the central position of IMD and the surrounding tissue with different volumes of IMD. It can be seen that, compared with surrounding tissue, a high-temperature region emerged on the skin surface at the position of IMD. Because of different heat generation rates, the high-temperature region is convex for the case of IMD with a width of 4 mm and is concave for the case of IMD with a width of 64 mm. Therefore, that is the reason for the trend, as depicted in Fig. 5. In this part, the information about the IMD outline can be clearly depicted by the area of the distinct temperature region; therefore, the soundness and the deformation of the IMD appearance can be further deduced.

3. Different IMD thermal conductivity

There are quite strict requirement for the material adopted by IMD, such as high mechanical strength, outstanding leakproofness, the electric insulation between circuit and biological tissue, excellent biological compatibility, and so on. At present, the commonly used materials can be classified into two kinds: one is provided with low thermal conductivity, such as silastic or polyethylene, and the other is provided with high thermal conductivity, such as titanium, stainless steel, cobalt alloy, and so on.²⁷ Since thermal conductivity is a major parameter in heat transfer and diversiform materials can be adopted by different IMD, the effect on skin surface temperature distribution due to different thermal conductivities also exists. Therefore, with a dimension of IMD of $32 \times 32 \times 4$ mm³, several thermal conductivities of IMD—which is, respectively, defined as 25, 10, 7.44, 0.5, 0.25, and 0.05 W/K m—are adopted in calculation to test the effect. At the same time, other parameters keep identical to each other.

Figure 6 denotes the temperature difference on the skin surface between the central position of IMD and the surrounding tissue with different thermal conductivities of IMD. And the results displayed in Figs. 7(a) and 7(b) are, respectively, the steady-state temperature distribution on the skin surface with different thermal conductivities. It is apparent that when the thermal conductivity of IMD is 25 W/K m, the skin surface temperature distribution is concave; when the thermal conductivity of IMD is 0.05 W/K m, the skin

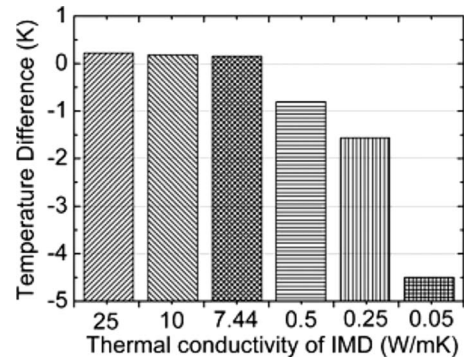


FIG. 6. Temperature difference on the skin surface between the central position of IMD and surrounding tissue with different thermal conductivities of IMD.

surface temperature distribution is convex. It can be easily concluded that while the thermal conductivity of IMD is higher than the tissue, a high-temperature region will take on the skin surface and the higher the thermal conductivity, the larger the temperature difference; on the contrary, while the thermal conductivity of IMD is lower than the tissue, a low-temperature region will appear on the skin surface and the lower the thermal conductivity, the higher the temperature. Therefore, in this case, while the thermal conductivity of the implanted IMD is higher than the tissue, if there is not a high-temperature region to appear at the skin surface, maybe the IMD is under some abnormal state.

4. Different IMD heat generation

Those IMDs that possess electrical energy are often provided with different running voltages and impedances; fur-

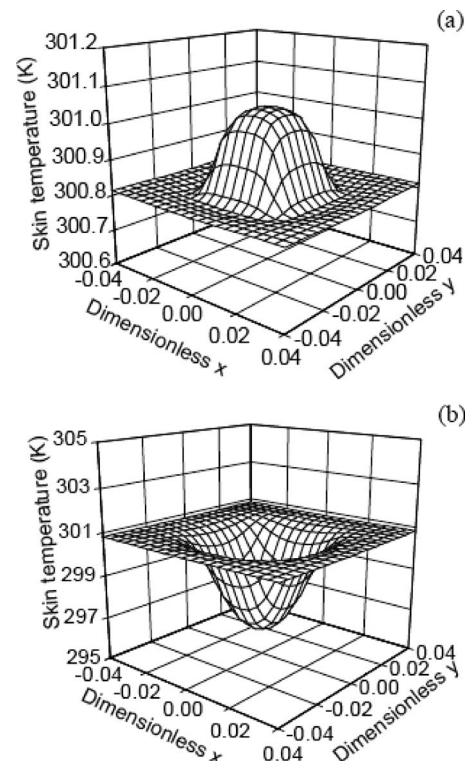


FIG. 7. Temperature distribution on the skin surface: (a) thermal conductivities of IMD 25 W/K m and (b) thermal conductivities of IMD 0.05 W/K m.

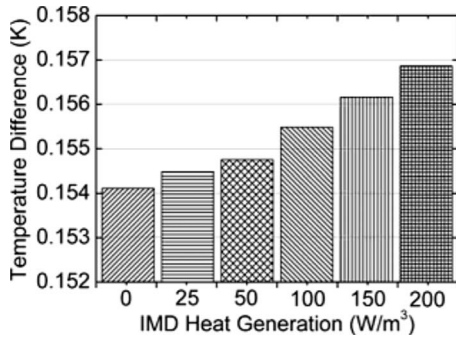


FIG. 8. Temperature difference on the skin surface between the central position of IMD and surrounding tissue with different heat generation rates of IMD.

ther, the heat generation during working will differ from each other. At the same time, the IMDs without electrical energy consumption will not have any heat generation. Therefore, different heat generations as prescribed as 0, 25, 50, 100, 150, and 200 W/m³ will be applied into the calculation to reveal the influence on the skin surface temperature distribution. Similarly, other parameters remain identical to each other.

Figure 8 depicts the temperature difference on the skin surface between the central position of IMD and the surrounding tissue with different heat generations of IMD. Clearly, no matter how much the heat generation is, the temperature difference always exists. And the stronger the heat generation, the larger the temperature difference. In this situation, while the IMD is provided with certain heat generation on its normal working state, consequently the maximum temperature on the distinct temperature region should be a constant. If the IMD is terminated due to the battery exhaustion or short circuit, the corresponding change would occur on the heat generation, which will lead to the shifting on the maximum temperature of the distinct temperature region. Therefore, one can make some judgment on the working state of the IMD.

C. Effect of external factors on skin surface temperature distribution

1. Physiological states

In daily life, when a person takes on various physiological states, there exists difference between the physiological parameters. For example, the blood perfusion and metabolic heat generation, which have important impact on the temperature distribution in biological bodies, are widely different when a person is under different physiological activities. There exists a correlation between these two parameters²⁹ $W_q = \omega_b / Q_m = 1 \times 10^{-3}$ kg/J, where ω_b is the blood perfusion and Q_m is the metabolic heat generation rate. W_q is the ratio of ω_b to Q_m . Figure 9 gives the temperature differences on the skin surface between the central position of IMD and the surrounding tissue by using different blood perfusion and metabolic heat generation rates. It suggested that the lower the blood perfusion and metabolic heat generation rates, the higher the temperature difference on the skin surface can be

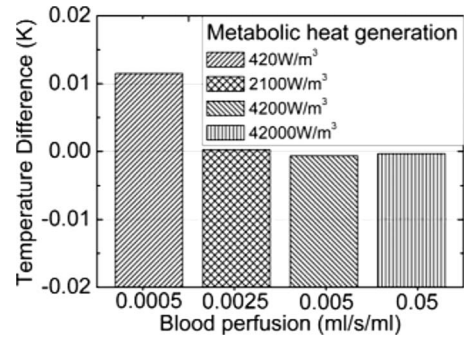


FIG. 9. Temperature difference on the skin surface between the central position of IMD and surrounding tissue in different blood perfusion and metabolic heat generation rates.

formed. As a result, when the human body is under normal physiological states, it is the most suitable situation for the work of such assessment method.

Otherwise, if the IMD is not compatible with the surrounding tissue, both the blood perfusion and metabolic heat generation rates in the surrounding tissue will not be the normal value. As displayed in Fig. 10(a), the red region with 4 mm width around the green IMD is the muscle tissue with disordered metabolism. The blood perfusion and metabolic heat generation rates in this red region are, respectively, 0.05 ml/s ml and 42 000 W/m³, and in the rest of the muscle tissue are, respectively, 0.05 ml/s ml and 4200 W/m³. Compared with Fig. 3(b), it is obvious that, on the skin surface, both the area of the high-temperature region and the temperature difference between the central position

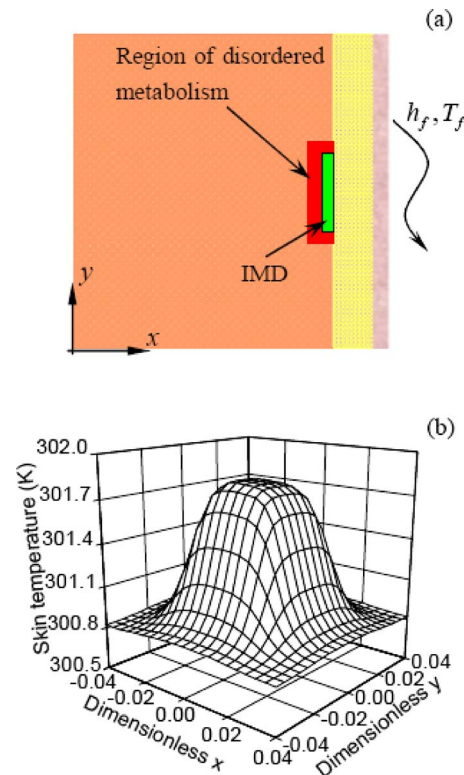


FIG. 10. (Color online) (a) Sketch of the calculation setup for the disordered metabolic region and (b) temperature distribution on the skin surface with the disordered metabolic region.

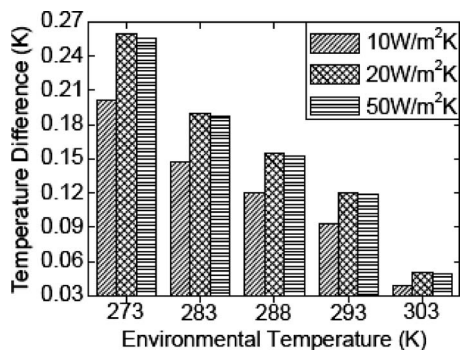


FIG. 11. Temperature difference on the skin surface between the central position of IMD and surrounding tissue. Implantation depth: $x=0.07$ m; $h_f=10, 20, 50$ W m⁻² K⁻¹; and $T_f=273, 283, 288, 293, 298, 303$ K, respectively.

of IMD and the surrounding tissue are much larger in Fig. 10(b). It would give out some clue to assess the compatibility between the implanted IMD and the surrounding tissue.

2. Environmental conditions

To test the effects of various environmental conditions, more simulations were also made by setting the heat transfer coefficients as 10, 20, and 50 W/m² K and treating the environmental temperatures as 273, 283, 288, 293, and 303 K, respectively. The calculated results are presented in Fig. 11.

Clearly, for the same heat transfer coefficient, the largest temperature difference between the central location of IMD and the surrounding tissue occurred in the case with the lowest environmental temperature of 273 K. Under the same temperature, the largest temperature difference appears in the case with the middle heat transfer coefficient as 20 W/m² K. Overall, the maximum temperature difference has been found as 0.26 K with 20 W/m² K heat transfer coefficients in 273 K environment, which is most beneficial for the detection of a far-infrared thermal imaging system.

Overall calculations denote that, for each character of IMD such as implanted depth, outline, thermal conductivity, and heat generation, as long as one of them takes on a change, the skin surface temperature distribution would be influenced evidently. Meanwhile, the physiological states and environmental condition also contribute impact on it. Therefore, various situations of the implanted IMD can be displayed on the skin surface temperature distribution which demonstrates that various assessments of IMD can be achieved through the different skin surface temperature distributions. In other words, it means a highly feasible IMD assessment through the infrared thermographs detected by far-infrared thermal imaging system. A further experimental investigation will be carried out to verify the concept proposed in this paper.

IV. EXPERIMENTS AND RESULTS

A. Experiments *in vitro*

Based on the above numerical simulation, a self-heating aluminum block as depicted in Fig. 12(a) has been adopted as the IMD to evaluate the method proposed in this paper, and then to preliminarily verify the results as predicted

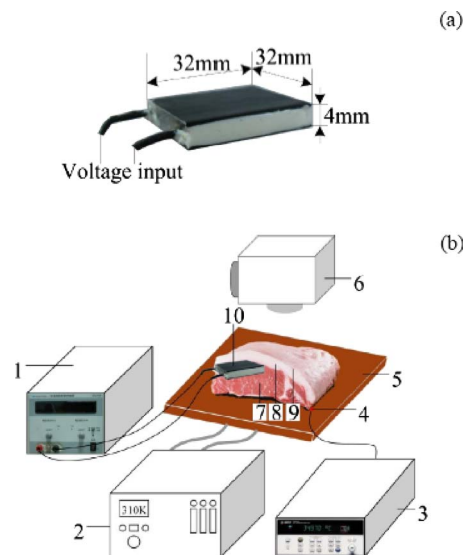


FIG. 12. (Color online) (a) Sketch of the heating aluminum block as an IMD and (b) sketch for *in vitro* experiment. (1) DC power supply, (2) thermostat water bath, (3) data acquisition system, (4) thermocouple, (5) copper plate, (6) medical far-infrared thermal imaging system, (7) tissue layer of the pork, (8) fat layer of the pork, (9) skin layer of the pork, and (10) the heating aluminum block which simulates the IMD.

above. This piece of heating aluminum block is a $30 \times 30 \times 5$ mm³ aluminum cube inserted with heat resistance which is formed by three 3 k Ω resistors in series. And the RTV silicone rubber produced by Liyang Kangda Chemical Co., Ltd. gives a good seal around the aluminum cube.

In addition, we prepared one piece of pork with a size of $80 \times 60 \times 80$ mm³. The thicknesses of the skin layer and fat layer are, respectively, 2 and 10 mm. In order to simulate the thermal state of the human body, a copper plate connected with a thermostat water bath at a temperature of 310 K was placed underneath the muscle tissue of the pork and the surface skin is exposed to the room environment, as shown in Fig. 12(b). The IMD was embedded into this piece of pork parallelly with the skin surface. Adiabatic material was used to wrap the four lateral surfaces of the pork. In the experiment, a thermocouple connected with the data acquisition system (Agilent 34970, USA) was mounted at the copper surface for monitoring the temperature. Meanwhile, the dc power supply (DH1720A-1, CN) and commercially available medical far-infrared thermal imaging system (HR-II, Institute of Optics and Electronics of North China, Beijing, China) are adopted in the experiment.

The actual environmental temperature is measured as 293 K. When a stable temperature distribution is formed in the pork, the IMD without electrification was embedded into the muscle tissue with its top side positioned at the interface between the fat and muscle tissue. After the stable temperature distribution was formed again, the medical far-infrared thermal imaging system begins to detect the temperature distribution on the skin surface of the pork. In the experiment, a metal wire is employed to demonstrate the location of the IMD. As shown in all the infrared thermographs, the middle region is the skin surface of the pork, the surrounding region is the adiabatic material, and the blue pane is dedicated to display the shape of the IMD. In Fig. 13, no matter if the

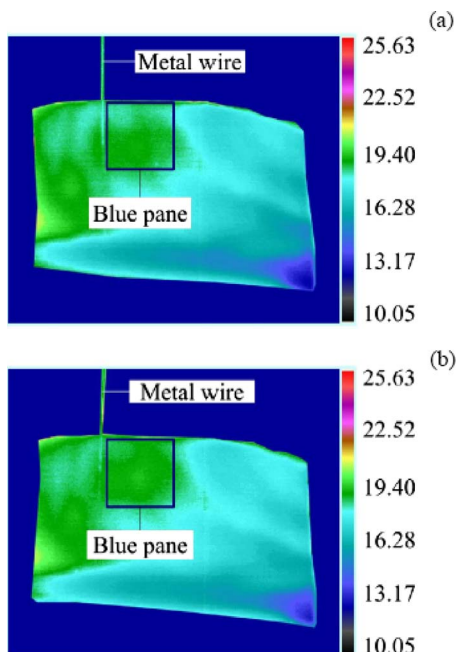


FIG. 13. (Color online) Infrared thermographs on the skin surface of the pork ($^{\circ}\text{C}$): (a) IMD without electrification and (b) IMD with electrification and the voltage input is 3 V.

voltage input is imposed on the IMD or not, there always exists a high-temperature region on the skin surface at the position of IMD. And the temperature differences on the skin surface between the central position of IMD and the surrounding tissue are, respectively, 1.05 K without electrification and 1.47 K with 3 V voltage input.

In order to achieve a more rapid and accurate measurement on the implanted IMD, alcohol was poured on the surface of the pork. At the same time, the IMD is under 3 V voltage input, and the change in infrared thermographs for 3 min is displayed in Fig. 14. Compared to Fig. 13(b), it can be found that the profile of the high-temperature region caused by the IMD is much clearer in Fig. 14. And other high-temperature region appeared in Fig. 13(b) either disappears or is cooled by the volatilization of alcohol. Clearly, a much

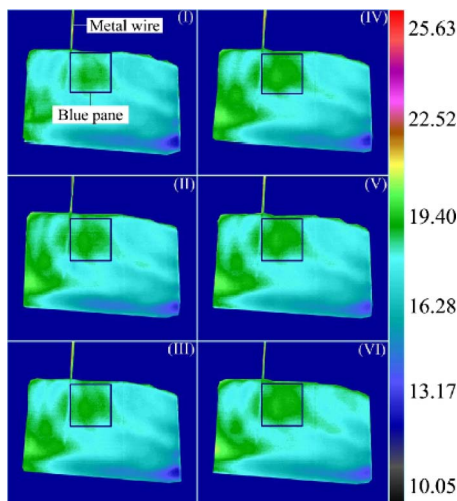


FIG. 14. (Color online) Infrared thermographs on the skin surface of the pork ($^{\circ}\text{C}$).

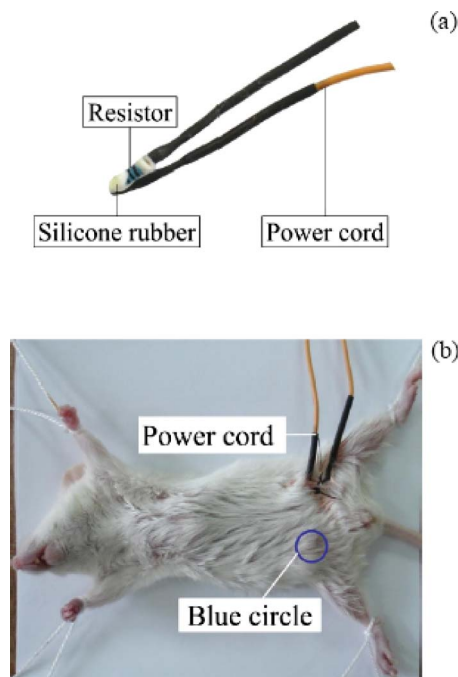


FIG. 15. (Color online) (a) Sketch of the resistor as an IMD and (b) picture of the mouse after implantation and the blue circle indicates the position of the IMD.

evident improvement on the infrared thermographs has been realized due to intentionally applied alcohol cooling.

Overall, several aspects of the experimental result accord well with the numerical simulation. First, the location of the IMD can be presented on the infrared thermograph. Second, no matter if there is heat generation or not, the temperature difference caused by the IMD always exists on the skin surface and the stronger the heat generation the larger the temperature difference. Third, the thermal conductivity of aluminum is much higher than the tissue and a high-temperature region indeed appears on the surface of the pork. However, because the experiment is performed *in vitro*, there are no blood perfusion and metabolic heat generation rates in the pork. And the material of IMD is quite different from the simulation. Therefore, under the similar boundary condition, there exists somewhat a difference between the theoretically predicted temperature differences and the experimental measurements, which can be accepted. These results indicate that the numerical simulation does provide a good overview on the effect of an implanted IMD produced on the skin surface temperature distribution, which may help assess each character of the IMD. Meanwhile, recur to the intentionally applied alcohol cooling, significant improvement on the speed and accuracy of the measurement can still be achieved.

B. Experiments *in vivo*

To further demonstrate the present method of using far-infrared thermal imaging system for the IMD assessment, *in vivo* experiments are also carried out subsequently. A BALB/C mouse weighing 23 g was selected, and the experimental setup is identical to that *in vitro*, besides the IMD which is one piece of resistor with 1 k Ω sealed by the RTV silicone rubber [as shown in Fig. 15(a)]. Before the experi-

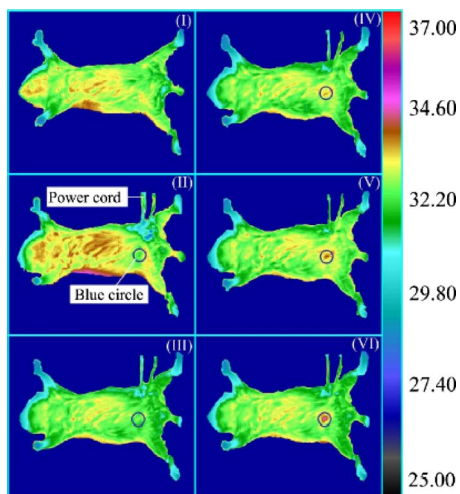


FIG. 16. (Color online) Far-infrared thermographs of the experiment *in vivo* ($^{\circ}\text{C}$).

ment, the mouse was fed for 2 months in standard laboratory conditions with free water and food. All procedures performed complied with the International Laboratory Animals Care Convention.

Before implanting the IMD, the mouse is administered with anesthesia via intraperitoneal injection of 6.7 mg/ml pentobarbital sodium. While the body temperature of the mouse will decrease markedly after anesthesia,³⁰ in order to maintain the normal body temperature, the mouse was gently fixed on the 310 K thermostat copper plate after falling into the state of general anesthesia. Then start the medical far-infrared thermal imaging system to detect the temperature distribution of the mouse. When a stable and normal temperature distribution is formed, the implantation can be processed. For the implantation, the abdomen of the mouse is disinfected, and a narrow opening on the right and lower abdomen with a length of 0.01 m is made with caution. The disinfected IMD is implanted into the abdomen from this narrow opening, and a suture is subsequently given to close the narrow opening after finishing the implantation. The picture of the mouse after implantation is displayed in Fig. 15(b), and the blue circle is the position of the IMD. At the same time, the far-infrared thermal imaging system keeps on detecting.

As depicted in Fig. 16, the infrared thermographs, respectively, represent the following states: (I) before implantation, (II) after implantation but no voltage input on the IMD, (III) 3 V voltage input on the IMD, (IV) 5 V voltage input on the IMD, (V) 6 V voltage input on the IMD, and (VI) 10 V voltage input on the IMD. The two lines next to the mouse body is the power wire of the IMD, and the blue circle is dedicated to display the location of the IMD.

It is apparent that when the IMD is implanted into the abdomen, the temperature distribution of the mouse takes on a change. In infrared thermograph (II), a low-temperature region appears at the location of IMD because of no voltage input and low thermal conductivity of the IMD, and the temperature difference between the central location of the IMD and the surrounding tissue is about 0.4 K. In infrared thermograph (III), due to the 3 V voltage input imposed on the

IMD, the low-temperature region shifts to a high-temperature region where the temperature difference to the surrounding tissue is about 0.4 K. If keeping increase in voltage input, both the area of the high-temperature region and the temperature difference to the surrounding tissue grow. The temperature differences to the surrounding tissue of 5, 6, and 10 V voltage inputs are, respectively, 0.85, 1.43, and 2.27 K. Because of the mouse hair, the experiment with intentionally applied alcohol cooling is not executed.

For the experiment *in vivo*, it is interesting enough that all the results accord well with the numerical simulation and the experiment *in vitro*, such as the location of the IMD can be presented on the infrared thermograph. Temperature difference caused by the embedded IMD always exists on the skin surface no matter if there is heat generation or not, a low-temperature region emerges on the skin surface due to the low thermal conductivity of the IMD and no voltage input, and so on. What deserves special mention is that the low-temperature region in infrared thermograph (II) translates to be a high-temperature region after imposing a voltage input on the IMD and the higher the voltage input the higher the temperature difference to the surrounding tissue.

To sum up all the theoretical analysis, numerical simulation, and the experiments both *in vitro* and *in vivo*, it is indeed feasible that the far-infrared thermal imaging system can be adopted in the state assessment of the implanted IMD.

V. DISCUSSIONS

The analysis, calculation, and experiments as given above revealed that once the IMD is embedded into the human body, the temperature distribution on the skin surface above the implantation location always distinguished from the surrounding tissue. In other words, there exists an abnormal region of temperature on the skin surface at the location which is related to implantation depth, volume, thermal conductivity, heat generation of the IMD, and the compatibility with surrounding tissue, respectively. Meanwhile, the physiological states and environmental conditions will also have impact on the abnormal region of temperature.

Based on the above results, the far-infrared thermal imaging system, which is a conventional instrument for detecting the skin surface temperature, is adapted to monitor the abnormal region of temperature on the skin surface caused by the IMD. And the IMD assessment can be executed by the information offered from the infrared thermographs.

When this assessment method is adopted to conduct a regular test for the IMD, it needs to complete the following steps: first, confirming all the information about the IMD, such as size, thermal conductivity, heating power, and so on; then collecting and preserving the initial infrared thermograph on the skin surface of the implantation location after implanting the IMD. After obtaining the initial infrared thermograph, one can deduce all the information about the implanted IMD. For example, if the IMD is implanted near the superficial skin, while the thermal conductivity of IMD is higher than the tissue, the abnormal region appears as a high-temperature region. In the following detection, one just needs to obtain the infrared thermograph on the same posi-

tion and compare it with the initial state. Consequently, the relevant results can be figured out. In order to avoid the measurement error caused by different physiological states of the human body and the environment, the detection should be completed under the condition that will ensure the same physiological states and the environment as far as possible, such as taking on the detection in a room with constant temperature and humidity and on the same time in each detection day.

In the infrared thermograph, not only the horizontal position of the IMD can be depicted by the abnormal region but also the implantation depth can be revealed by the temperature difference between the abnormal region and the surrounding tissue. The shape of the abnormal region in the infrared thermograph can also show whether there is a deformation of the IMD after implantation. At the same time, the abnormal region will be much more vivid while there is incompatible phenomenon between the IMD and the surrounding tissue.

For those IMDs which possess electrical energy, the running state and battery power loss can also be assessed by the information offered from the infrared thermographs. In the course of their work, there always exists some heat generation which is caused by both IMD itself and the power battery. When the IMD is in its proper condition, the heat generation caused by the IMD itself should be a constant value. Therefore, once there is an equipment failure, IMD may stop working and heat generation will disappear immediately. If short circuit occurs, the heat generation of IMD will be an absolutely higher value than the normal one. As a result, the main temperature of the abnormal region can be the clue for the state assessment of the IMD. At the same time, the lithium-iodine batteries, which is a common choice for the IMDs, possess general discharge characteristics: their output voltage level keeps constant up to the critical voltage and then falls sharply (in several months).^{3,31,32} Therefore, in battery-powered process, the heat generation of the batteries will have a change which can also be the clue for the battery power loss.

In order to achieve a more rapid and accurate measurement on the implanted IMD, the intentional cooling by alcohol on the skin surface may offer some help. In the experimental results, it can be found that the profile of the high-temperature region on the skin surface caused by IMD is much clearer and other high-temperature regions either disappear or be cooled by the volatilization of alcohol. Therefore, it does give a much evident improvement on the infrared thermographs.

In addition, the method proposed in this paper not only can achieve the state assessment of the IMD but also possess several advantages. First, the operating costs of the far-infrared thermal imaging system are much lower than other medical imaging systems. Second, all the detection and assessment completed will not provide any wound and radiation to the human body, which means that it is an assessment method with absolute security. Finally, the far-infrared thermal imaging system has been a mature technology nowadays, and the operation of the system is quite quick and convenient. Therefore, people with the implanted IMD can

fulfill the detection and assessment according to their wishes at any time. Once an abnormal phenomenon emerged, people can seek the medical advice immediately.

However, this method is not perfect. At present, although the highest thermal sensitivity of the far-infrared thermal imaging system all over the world is 0.02 K in the environment with 303 K,³³ it is an inaccessible value in the course of practical use. Therefore, the application of this method still has certain limitation. According to the numerical simulation, only when the IMD is embedded as close as possible to the superficial skin, the abnormal region of temperature on the skin surface will be more visible. In other words, this method is much more efficient to the IMD implanted near the superficial skin. Otherwise, normal physiological states and fitting environmental conditions are the indispensable qualifications to this method. The absence of one of both qualifications may lead to the failure in assessment.

VI. CONCLUSION

So far, significant progresses have been made on the material, function, structure, and design of the IMDs. Such devices are becoming more and more attractive which merge the medical functionality, convenience, and economy into one assembly to fulfill a wide variety of practical needs. They are playing an ever increasing role in modern advanced medical technologies.¹⁻¹⁰ There have been many practical assessment methods for such device. However, the patterns as justified in this paper showed certain complementary merits to the existing methods. Just using one piece of infrared thermographs, much information about the IMD can be interpreted.

In this study, theoretical interpretation and numerical simulations were preformed to evaluate the abnormal temperature distribution on the skin surface and thus its capability for detection by the far-infrared thermal imaging system. Parametric analyses were performed to test the effects of various typical characteristics of the IMD, physiological factors, and the environmental conditions. Particularly, with same implantation depth, the position of IMD can be displayed by the abnormal region of temperature on the skin surface. Either the area or temperature distribution of the abnormal region is unique due to different volumes of the IMD. The greater difference in thermal conductivity between the IMD and body tissue is more obvious for abnormal region. Large heat generation, incompatible phenomenon, favorable physiological states, and environmental conditions will also make the abnormal region vivid. Proof-of-concept experiments were conducted to further demonstrate the feasibility of using far-infrared thermal imaging system to assess the IMD. At the same time, externally imposed alcohol cooling was introduced as a flexible way to improve the speed and accuracy of the detection.

However, all the works presented in this paper are only contributed to demonstrate the feasibility of the alternative assessment method to IMD. The specific assessing index and standard still needs to be developed in future works.

ACKNOWLEDGMENTS

This work is partially supported by Tsinghua-Yue-Yuen Medical Sciences Fund and the NSFC grant under Contract No. 50776097.

- ¹W. Irnich, *PACE* **25**, 1235 (2002).
- ²M. Gerritsen, A. Kros, V. Sprakel, J. A. Lutterman, R. J. M. Nolte, and J. A. Jansen, *Biomaterials* **21**, 71 (2000).
- ³J. Vounckx, N. Azemard, and P. Maurine, *Lect. Notes Comput. Sci.* **4148**, 292 (2006).
- ⁴J. H. Niu, Y. F. Liu, Q. S. Ren, Y. Zhou, and S. Niu, *Sci. China Ser. F, Inf. Sci.* **51**, 101 (2008).
- ⁵P. K. Mason, M. A. Wood, D. B. Reese, J. H. Lobban, M. A. Mitchell, and J. P. DiMarco, *Am. J. Cardiol.* **92**, 1127 (2003).
- ⁶X. J. Wei and J. Liu, *Front. Energy Power Eng. China* **2**, 1 (2008).
- ⁷Y. Yang, X. J. Wei, and J. Liu, *J. Phys. D: Appl. Phys.* **40**, 5790 (2007).
- ⁸J. W. Moore III, W. Barrington, R. Bazaz, S. Jain, J. Nemeč, O. Ngwu, D. Schwartzman, A. Shalaby, and S. Saba, *Int. J. Cardiol.* (in press).
- ⁹Q. F. Liang, L. Yuan, W. J. Wang, S. J. Cao, L. L. Liu, Y. P. Zhu, L. S. Wang, N. Z. Yao, and B. C. Quan, *Chin. J. Clinical Anatomy* **23**, 664 (2005).
- ¹⁰J. F. Xian, Y. X. Li, F. Y. Man, B. Wang, Z. L. Liu, Z. C. Wang, and D. M. Han, *Chin Arch Otolaryngol Head Neck Surg* **14**, 389 (2007).
- ¹¹M. L. Zuo, L. X. Yin, C. M. Li, A. G. Luo, Y. Deng, L. J. Cheng, S. Li, S. Wang, Y. Yu, T. Laske, Y. Zhao, and N. Skadsberg, *Chin J Med Ultrasound* **2**, 200 (2005).
- ¹²Y. Z. Huang, S. T. Ren, J. Long, J. H. Zhou, X. C. Liu, and X. G. Kong, *Chin. J. Med. Imaging Technol.* **22**, 1567 (2005).
- ¹³A. Mazur, M. E. Anderson, S. Bonney, and D. M. Roden, *J. Am. Coll. Cardiol.* **37**, 1100 (2001).
- ¹⁴D. M. Newman, P. Dorian, M. Paquette, N. Sulke, M. R. Gold, D. S. Schwartzman, K. Schaaf, K. Wood, and L. Johnson, *Am. Heart J.* **145**, 841 (2003).
- ¹⁵G. Lin, R. A. Nishimura, H. M. Connolly, J. A. Dearani, T. M. Sundt III, and D. L. Hayes, *J. Am. Coll. Cardiol.* **45**, 1672 (2005).
- ¹⁶D. L. Wan, S. Z. Wang, H. L. Li, Z. P. Chen, and Y. Kuang, *Int. J. Ophthalmology* **4**, 445 (2004).
- ¹⁷C. Ermis, A. X. Zhu, S. Pham, J. M. Li, M. Guerrero, A. Vrudney, L. Hiltner, F. Lu, S. Sakaguchi, K. G. Lurie, and D. G. Benditt, *Am. J. Cardiol.* **92**, 815 (2003).
- ¹⁸P. K. Mason, M. A. Wood, D. B. Reese, J. H. Lobban, M. A. Mitchell, and J. P. DiMarco, *Am. J. Cardiol.* **92**, 1127 (2003).
- ¹⁹Z. L. Liu and M. L. He, *Chinese J. Oral Implantol.* **3**, 78 (1998).
- ²⁰H. P. Song, Q. Liu, L. Yuan, and X. B. Li, *Orthopedic J. China* **14**, 1560 (2006).
- ²¹B. Y. Mao, T. Huang, Z. Z. Ying, C. X. Li, and Q. M. Si, *Orthopedic J. China* **15**, 110 (2006).
- ²²J. Drori, U.S. Patent No. 6,154,012 (28 November 2000).
- ²³H. H. Pennes, *J. Appl. Phys.* **1**, 93 (1948).
- ²⁴Z. S. Deng and J. Liu, *ASME J. Biomech. Eng.* **124**, 638 (2002).
- ²⁵M. N. Ozisik, *Heat Conduction* (Wiley, New York, 1980), p. 225.
- ²⁶Z.-S. Deng and J. Liu, *Comput. Biol. Med.* **34**, 495 (2004).
- ²⁷B. H. Wang, *Chinese Journal of Medical Instrumentation* **13**, 287 (1989).
- ²⁸FLUENT User's Guide, Fluent Inc. (2006).
- ²⁹J. Liu and C. Wang, *Bioheat Transfer* (Science, Beijing, 1997), p. 344, in Chinese.
- ³⁰H. Zhang, Y. Yang, J. Liu, and Z. S. Deng, *Science & Technology Rev.* **26**, 66 (2008).
- ³¹G. Pistoia, *Batteries for Portable Devices* (Elsevier, Amsterdam, 2005), p. 55.
- ³²T. Atwater, IEEE MILCOM'94 Conference Record, 1994 (unpublished), Vol. 1, p. 203.
- ³³<http://www.flir.com.cn/sc3000.htm>.